ARMA 14-7371

# Flow of dense suspensions through fractures: Experimental and computational observation of velocity-field heterogeneity

Medina, R. and Elkhoury, J.E. and R. L. Detwiler
*Department of Civil and Environmental Engineering, University of California, Irvine, California, USA.*
Morris, J.P., and Prioul, R.
*Schlumberger-Doll Research Center, Cambridge, Massachusetts, USA.*
Desroches, J.
*Services Pétroliers Schlumberger, Paris, France.*



This paper was prepared for presentation at the 48th US Rock Mechanics / Geomechanics Symposium held in Minneapolis, MN, USA, 1-4 June 2014.



**ABSTRACT:** We conducted experiments in which a high concentration (50% v/v) of granular solids suspended in a non-Newtonian carrier fluid (0.75% guar gum in water) flowed through a parallel-plate fracture. Digital imaging and particle-image-velocimetry analysis provided a detailed map of velocities within the fracture. Results demonstrate development of a strongly heterogeneous velocity field within the fracture. We observed the highest velocities along the no-flow boundaries of the fracture and the lowest velocities along the centerline of the fracture. Computational fluid dynamics (CFD) simulations using a recently developed model of the rheology of dense suspensions of mono-disperse solids in Newtonian carrier fluids closely reproduced experimental observations of pressure gradient versus flow rate. Results from additional simulations suggest that small (3%) variations in solid volume fraction within the fracture could lead to significant (factor of two) velocity variations within the fracture with negligible changes in observed pressure gradients. The variations in solid volume fraction persist over the length of the fracture, suggesting that such heterogeneities may play a significant role in the transport of dense suspensions. Our work suggests that a simple average conductivity parameter does not adequately represent the flow of high solid content suspensions in a fracture, as the flow develops strong three-dimensional structure even in a uniform rectangular channel.

## 1. INTRODUCTION

Flow of fluids with high concentrations of suspended solids are important to a range of problems. Examples include magma composed of crystals suspended in silicate melts [1] and fluids used for hydraulic fracturing for oil and gas production [2,3] and environmental remediation [4]. These fluid-solid suspensions typically behave as a fluid with very different rheology than the solids-free carrier fluid [5]. At high shear rates, the presence of the solid typically causes shear-thinning behavior, whereas at low shear rates, a yield stress is common. Thus, flow of high-solid-volume-fraction fluids in porous and fractured media defy simple relationships between applied pressure gradient and flow rate as observed for Newtonian fluids.

Studies of viscous flow of fluids with high solid-volume-fraction (SVF) in geometries relevant to subsurface systems include flow through tubes [6] and parallel-sided channels [7]. In parallel-sided channels, frequently used as analogs to fractures, experimental results show that, even if the carrier fluid is Newtonian, the velocity field deviates from the classic parabolic profile as a result of the nonuniform distribution of solids across the gap between the surfaces. For dilute suspensions, the mixture behaves as a Newtonian fluid with viscosity that increases with solid fraction [8], but for dense suspensions, a plug of high solid fraction fluid forms in the middle of the flow field with lower solid fraction and lower viscosity regions near the wall [7]. These dense suspensions typically exhibit a yield stress as the jamming limit is approached, which occurs when the solid content approaches the random packing limit [9].

Previous experimental studies of the flow of granular suspensions through channels or slots focused on the interaction of fluids and particles and the resulting influence on the velocity profile across the gap between the channel surfaces. At larger scales, the potential for segregation of solids, resulting in variable SVF within the flow field (in the fracture plane), may lead to

variability in local effective viscosity and instabilities within the flow field [10]. Though a range of different models have been used to represent flow of various non-Newtonian fluids in confined geometries, these models do not account for the potentially significant variability in fluid rheology that results from variations in solid volume fraction. Recently, Lecampion and Garagash [5] presented a detailed model for the flow of dense suspensions through confined geometries (tubes and channels). They also considered a lubrication theory limit that does not explicitly represent the velocity distribution across the gap of a fracture. This simplified model can be applied at larger scales to investigate the in-plane velocity variations within a fracture caused by variability in solid volume content in the fracture plane.

We present results from a pair of experiments in which we flowed high-SVF fluid through the same parallel-sided fracture with two different boundary-condition configurations. To aid in interpreting the results of the experiments, we simulated flow through the experimental system using the rheological model of Lecampion and Garagash [5]. We focus on conditions where suspended solids flow with the fluid, and we do not explore the regime where settling of solids within the fracture is important.

## 2. OVERVIEW OF EXPERIMENTS

We designed an experimental apparatus to explore the role of high-SVF fluid properties and flow geometry on fracture flow. Transparent parallel-sided fractures provide the ability to both directly measure the flow geometry under experimental conditions and visualize and quantify the velocity field within the fracture. Here, we describe the experimental apparatus, the details of the fluid-solid mixture used for the experiments, and the procedure used to carry out the experiments.

### *2.1. Experimental apparatus*

A rotating stand rigidly mounts a high-sensitivity charge-coupled device (CCD) camera (Photometrics Quantix KAF-6303e) above a monochromatic (red) LED panel. Clamps hold the fracture cell to the stand between the light source and the camera. The fracture cell secures the fracture plates with a fixed space between the surfaces and allows light transmission through the entire flow field. The fracture surfaces (15 cm × 15 cm × 1.2 cm smooth glass plates) are separated by two aluminum shims which act as no-flow boundaries along the fracture edges and provide a uniform fracture aperture of ~0.3cm. Two 2.5 cm-thick fused-quartz windows supported by 2.5 cm-thick aluminum frames clamp the fracture surfaces together (Fig. 1). An electronic controller synchronizes 65 ms pulses of the LED panel with exposure of the CCD to provide reproducible images of the fracture. The CCD camera uses 12-bit digitization of the measured intensities in images with 76 μm pixels. Section 3 describes processing of the measured intensities.

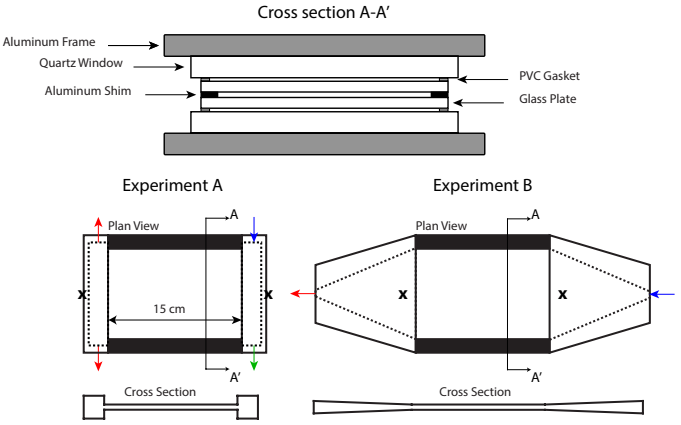


Fig. 1. Schematic of inlet and outlet manifold configuration for Experiments A (left) and B (right), and cross-section A-A' of fracture cell for both experiments (top). The separate schematics shown for Experiment A and B highlight the difference between the manifold geometries for the two experiments. For Experiment A, a large rectangular channel (much more conductive than the fracture) bounded each end of the fracture. For Experiment B, the manifold gradually tapered from the inlet/outlet tubing to the fracture geometry. The schematic shows the location of the inlet (blue arrows), outlet (red arrows), and waste (green arrow; experiment A only). The black crosses mark the locations of the pressure ports, which were connected to the differential pressure transducer.

We carried out two experiments in the same fracture with different inlet/outlet boundary conditions. Experiment A used linear inlet and outlet manifolds (Fig. 1) that included large rectangular channels that spanned both ends of the fracture. Initially, a high-capacity syringe pump pushed slurry into one end of the inlet manifold (blue arrow) and out a waste line at the other end of the inlet manifold (green arrow) filling the manifold with slurry. We then closed the waste line and opened the two outlets on either side of the outlet manifold (red arrows) to initiate flow through the fracture. Experiment B used a wedge-shaped manifold (Fig. 1) that allowed us to flow directly into the fracture without prefilling the manifold. This configuration included only a single inlet and a single outlet tube. Furthermore, the wedge-shaped manifold tapers gradually from the inlet port (blue arrow) to a slot with the same width ($W$) and aperture ($h$) of the fracture. A differential pressure transducer connected to the ports located at the center of the inlet and outlet manifolds (marked by Xs in Fig. 1) measured the differential fluid pressure across the fracture at high temporal resolution (0.3 Hz) during each experiment.

### 2.2. *Fluid description and experimental configuration*

For both experiments, we used a 0.75% mixture of guar gum and water as the carrier fluid. Guar is a shear thinning fluid that behaves as a Newtonian fluid under low shear rates and exhibits non-Newtonian, shear-thinning behavior at higher shear rates. We selected guar because it is a well-characterized high-viscosity fluid that can be prepared reliably and consistently as a base fluid for high-solid concentration slurries. A laboratory-grade blender (Waring 7012g) mixed the guar/water solution for at least 10 minutes to ensure complete hydration of the guar.

We prepared the high-SVF fluid by adding 50% (v/v) silica sand to the de-aired carrier fluid. The added sand had a multimodal particle size distribution ranging from submicron size to about 600 μm (Fig. 2). A rotary mixing paddle mixed the slurry as we slowly added sand to the container. A lid with a vacuum-tight pass-through for the mixing paddle sealed the container, and the paddle mixed the slurry under vacuum for approximately 15 minutes to ensure a well-mixed and degassed fluid.

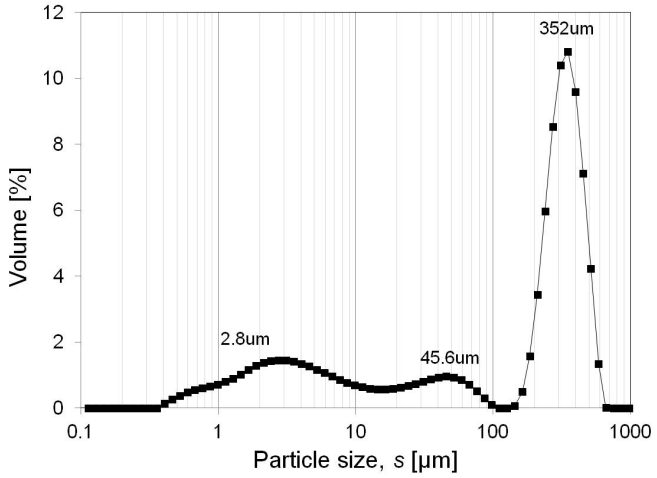


Fig. 2. Particle-size distribution for the solids used in the flow experiments. The solids consisted of angular quartz grains. The fines serve to reduce the permeability of the solids, which minimizes the tendency for jamming at low shear rates.

After mixing, we immediately transferred the slurry to the 2.5-liter syringe pump to minimize solid particle settling prior to initiation of the flow experiment. The syringe pump consisted of a clear polycarbonate pipe (1.7-m long, 2.5-cm inner diameter) fitted with a plunger from a 60-ml syringe. A plastic funnel secured to the bottom of the pipe provided a smooth transition from the 2.5-cm-inner-diameter pipe to 3-mm-inner-diameter tubing. Water pumped into the opposite end of the polycarbonate pipe at specified flow rates displaced the plunger and pushed slurry through the funnel and into the fracture.

### 2.3. *Experimental procedure*

Prior to initiating flow experiments, we used light-transmission techniques to measure the fracture aperture field. This involved two steps: (i) measuring the mean fracture aperture and (ii) measuring the spatial distribution of aperture within the fracture. To measure the mean aperture, we oriented the fracture vertically with the inlet at the bottom and filled the inlet tubing, manifold, and about 10% of the fracture with dyed water (FD&C Blue No. 1 at 32 mg/L, Warner Jenkins) and acquire a set of images. We then injected a measured volume of dyed water ($V_d$) to fill the fracture to about 90% and acquired another set of images. The difference in area between the images at 10% and 90% provides an area, $A_d$, occupied by the injected fluid volume ($V_d$) and the mean fracture aperture, $\langle h \rangle = V_d/A_d$. To quantify any variations in the fracture-aperture field, we acquired a set of images with the fracture completely filled with dyed water, flushed the fracture with ~10 pore volumes of deionized water, and acquired a set of reference images of the fracture filled with deionized water. After measuring the aperture field, we drained and dried the fracture and associated tubing prior to each flow experiment.

Flow experiments involved the following steps: (1) filling the inlet tubing with solids-free carrier fluid while taking care to avoid introducing any air bubbles that could introduce optical artifacts; (2) slowly filling the fracture carrier fluid and acquiring reference images of the carrier-fluid-filled fracture; (3) connecting the tube carrying high-SVF fluid to the inlet port on the manifold and rotating the fracture orientation to horizontal; (4) initiating image and data acquisition and flow of the high-SVF fluid at 6.0 ml/min; (5) increasing the light intensity when the fracture was uniformly filled with high-SVF fluid to enhance image resolution; and (6) initiating the stepped flow-rate experiment.

## 3. IMAGE ANALYSIS

Raw images consisted of measured light-intensity values which we transformed to light absorbance, $A = \ln\left(\frac{I_r}{I_i}\right)$, where $I_r$ is the measured intensity at a pixel in a reference image and $I_i$ is the measured intensity at the same pixel in the measured image. Using absorbance rather than intensity allows quantitative comparison of images between experiments by eliminating the influence of variations in camera or light-source settings. Additionally, absorbance fields provide greater contrast between flowing particles and the carrier fluid.

Preprocessing of images corrected for small registration errors and variations in emitted light intensity. The test stand included a small orifice located adjacent to the fracture that allows light to be transmitted from the light source to the camera. This region provided an

unobstructed measure of the light source intensity throughout the experiment and also served as a registration point. Preprocessing consisted of applying image registration and intensity normalization techniques described by Detwiler et al. [11].

### *3.1. Aperture measurement*

Light absorbance can be directly related to fracture aperture by applying the Beer-Lambert law to measurements of the fracture filled with clear and dyed water:

$$I = I_0 e^{-\mu C d + \xi} \quad (1)$$

where $I$ is the measured intensity at a location, $I_0$ is the incident light intensity, $\mu$ is the absorption coefficient of the solute, $C$ is the dye concentration, $h$ is the gap filled with the solute, and $\xi$ is a constant that accounts for absorbance by the solvent and the glass plates. Although the fracture consists of two pieces of flat glass, long wavelength variations due to imperfections in the glass fabrication process are possible. Additional aperture variations may be caused by small thickness variations in the aluminum shims that separate the fracture plates, as well as small variations in the torque applied to the bolts securing the aluminum frame. The aperture field measurement is computed using methods described in Detwiler et al. [11] and only briefly summarized here. Images of the fracture filled with clear and dyed water (described in Section 2.3) are registered and normalized as previously discussed. From the mean aperture $\langle h \rangle$ of the cell, where $\langle\rangle$ denotes a spatial average (see section 2.3), the aperture at any location is calculated as

$$h_{i,j} = \frac{A_{i,j}}{\langle A \rangle} \langle h \rangle \quad (2)$$

This method of measuring fracture aperture yields measurements of $h_{i,j}$ that are accurate to within approximately ±1% of $\langle h \rangle$, or about 30 μm for the fracture used in these experiments.

### *3.2. Particle image velocimetry*

Particle image velocimetry (PIV) analysis is performed using a modified version of the Matlab-based software, PIVlab [12]. A high-pass filter applied to the absorbance fields removes long wavelength features and increases contrast between individual sand grains and the surrounding carrier fluid. PIVlab divides the fracture into 40×40 pixel subregions and calculates the cross-correlation between corresponding subregions between two images. PIV analysis provides a measure of the average distance the sand grains move from one frame to the next. We perform PIV analysis on the entire dataset (thousands of images) and construct the time-series of particles moving within the cell.

## 4. EXPERIMENTAL RESULTS

After initializing flow of the slurry through the fracture, we carried out the two flow experiments by sequentially decreasing the flow rate through a sequence of steps and then increasing through a subset of the same flow rates. At each flow rate, we attempted to allow the system to reach steady state as measured by the pressure differential and effluent mass-flow-rate.

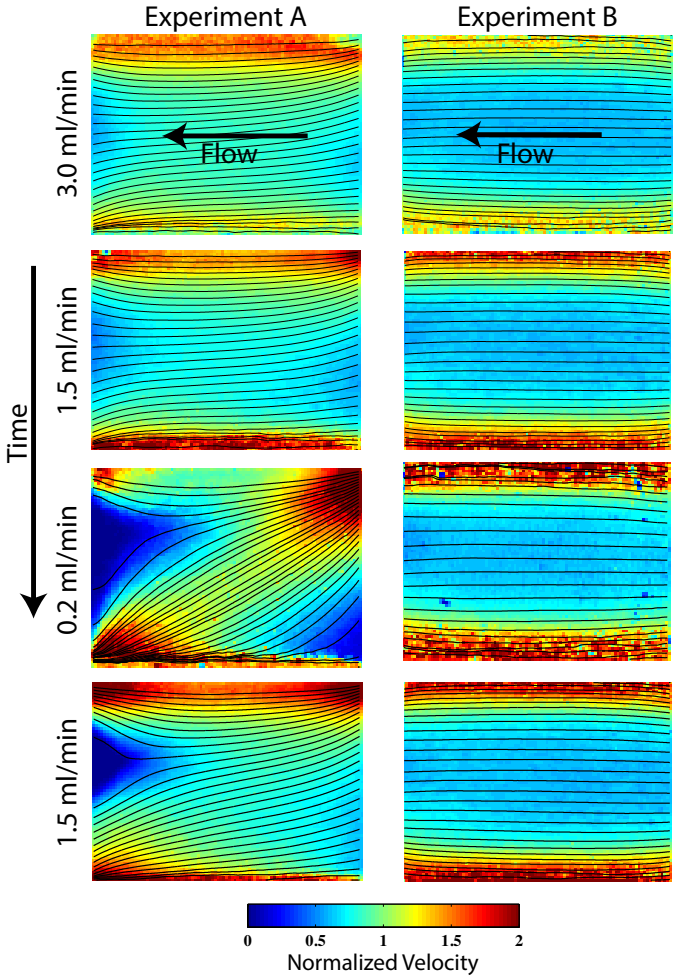


Fig. 3. Normalized velocity fields measured over the entire fracture for a subset of the flow rates for Experiments A and B superimposed with the velocity streamlines. The velocity fields are normalized by the depth-averaged velocity ($V$=$Q$/$W\langle h \rangle$, where $Q$ is the volumetric flow rate measured at the outlet, $W$ is the fracture width, and $\langle h \rangle$ is the mean fracture aperture) during each step to facilitate comparison of velocity fields and profiles at different flow rates. A jammed (~zero velocity) region developed in Experiment A. High-velocity regions/bands are observed in both experiments near the no-flow (top and bottom) boundaries.

PIV analysis of sequential image pairs provide discrete measurements of the velocity field within the fracture. Averaging sequential velocity fields measured during a period when the observed flow rate was approximately constant provides a relatively noise-free measure of velocity throughout the fracture at each flow rate. Figure 3 shows a representative subset of these velocity fields

for both experiments. During Experiment A at early time, the flow field was nearly one dimensional, with the somewhat surprising result that the highest velocities occurred along the no flow boundaries (top and bottom of each frame in Fig. 3). However, at later time, the flow field became more complex with a large region near the outflow boundary with zero velocity and a smaller region near the inlet boundary with near-zero velocity. When the flow rate returned to 1.5 ml/min (last frame at bottom), the inlet region returned to a similar configuration to the earlier measurement at the same flow rate (second frame from top), but the outlet region remained jammed. This hysteretic response is a direct manifestation of the geometry of the boundaries. Though the outlet manifold is much larger than the fracture aperture, such that pressure losses within the manifold are relatively small, a stagnation point at the middle of the manifold led to the development of the zero velocity region when shear rates decrease. The resulting jamming of the solids is not immediately reversible.

By contrast, the inlet and outlet boundaries for Experiment B preclude a stagnation point within the flow system. The result is that the flow field remains nearly one dimensional throughout the duration of the experiment. Furthermore, there is no evidence of hysteresis in the flow field due to the lack of jamming of the solids. However, as with Experiment A, the highest velocities occurred along the no-flow boundaries, which was, again, not expected. We explore the possible explanations for the strong in-plane variation in velocities observed in both experiments through computational simulations in the next section.

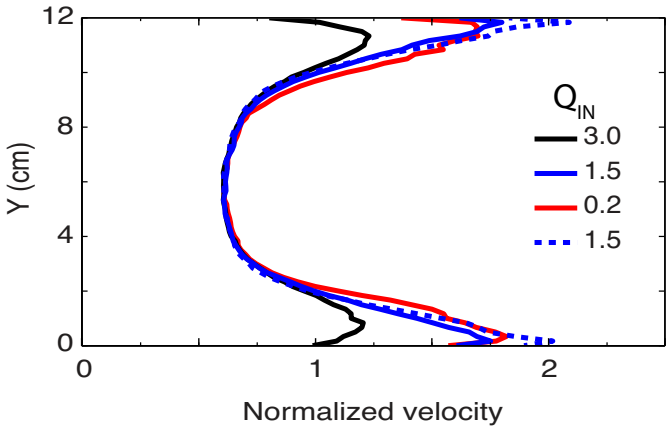


Fig. 4. Normalized velocity profiles corresponding to the velocity fields shown in the right column of Fig. 3. These are average profiles (over the fracture length) measured perpendicular to the flow direction. The velocity near the no-flow boundaries is approximately twice the velocity in the middle of the fracture.

Figure 4 shows velocity profiles plotted perpendicular to the flow direction and averaged over the length of the fracture and provides a more quantitative measure of the velocity distributions observed during Experiment B. The magnitude of the high-velocity channels along the edges of the fracture increase relative to the mean velocity as the flow rate decreases. In the following section, we simulate flow through the fracture to test possible explanations for the strong velocity heterogeneities observed within the uniform-aperture fracture.

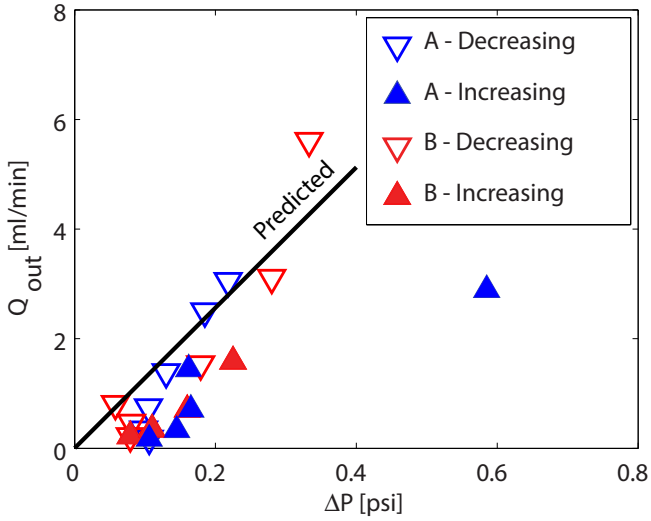


Fig. 5. Volumetric flow rate through the fracture ($Q$out) plotted against differential pressure ($\Delta P$) for the full range of measured flow rates for both experiments.

To interpret the transient behavior observed during the experiments, it is useful to plot effluent mass-flow-rate, $Q_{out}$, versus $\Delta P$ at different times during each experiment to clarify how the slurry rheology affects the transmissivity of the constant-permeability fracture. Figure 6 plots the observed values of $Q_{out}$ at the end of each steady flow-rate step against the corresponding value of $\Delta P$ for both Experiment A and B. Despite significant differences in the behavior of the time series of the two experiments, plots of $Q_{out}$ versus $\Delta P$ are surprisingly similar for both experiments. Most notably, results from both experiments suggest a yield stress as $Q_{out} \rightarrow 0$. Also, at the end of the experiments, when flow rate had been reduced to near zero and then increased, the two experiments exhibited significantly different behavior, highlighting strong hysteretic behavior in Experiment A.

## 5. COMPUTATIONAL SIMULATIONS

### *5.1. Fully developed homogeneous flow of high-solid-volume slurry between two plates*

We use a rheological model developed by Lecampion and Garagash [5] to predict the flow of wet granular media and dense suspensions. They considered the rheology of mono-disperse solids carried by a Newtonian fluid. Their model reproduces the regimes of dilute, intermediate, and very dense suspensions by combining an effective pressure dependent yield stress

(typical of granular media) with hydrodynamic stresses. Although Lecampion and Garagash [5] present a general transient rheological model, we will utilize the simpler result they obtained for fully developed flow between two plates. In this limit, they demonstrated that the total flux, $Q$, between horizontal plates is governed by the familiar "cubic law":

$$Q = W \frac{h^3}{12\mu} \frac{\Delta P}{L} \quad (3)$$

where $\mu$ is the apparent (width-averaged) viscosity of the slurry, $h$ is the aperture, $W$ is the width, and $L$ and $\Delta P$ are the length and pressure drop across the plates in the direction of flow, respectively. Lecampion and Garagash [5] found that $\mu$ can be related uniquely to the solid volume fraction of the slurry and the viscosity of the Newtonian carrier fluid, $\mu_c$, according to the relationship shown in Fig. 6.

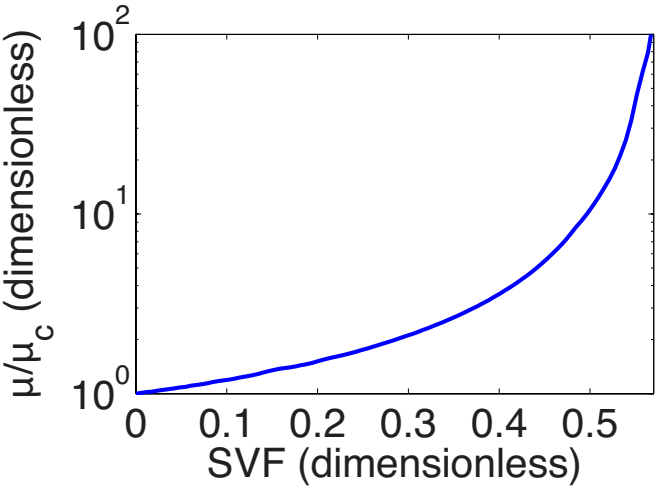


Fig. 6. The apparent (width-averaged) Newtonian viscosity, $\mu$, of fully developed slurry-flow between two plates can be predicted given the Newtonian viscosity, $\mu_c$, of the carrier fluid and the solid volume fraction (SVF) of the slurry [5].

The highest flow rate in the experiments corresponds to a strain rate of approximately 0.05 $s^{-1}$. Consequently, the experimental flow field is below the lowest shear rate measured; we can assume the guar-based carrier fluid is within its Newtonian regime, and we take its viscosity to be 8 Pa·s.

Let us now consider homogenous slurry, with 50% SVF, flowing between two plates with Newtonian carrier-fluid viscosity of 8 Pa·s. This results in a slurry with effective viscosity of 84.3 Pa·s (Fig. 6). Figure 5 compares the experimental observation with the model prediction of pressure difference between inlet and outlet as the flow rate is varied. The model and experiment are in excellent agreement for decreasing flow rate (down triangles) for both experiments A and B. The experimental results show some evidence of a yield stress (approaching zero flow at finite pressure differential).

While we are able to obtain good agreement with the total flux and pressure drop, the experimental results indicate significant variations in the velocity field within the slot. In the following sections, we present an approach for capturing the details of a heterogeneous flow field and attempt to explain the experimentally observed flow structure.

### *5.2. Simulations of heterogeneous flow in a slot*

Both experiments develop nonuniform flow fields, despite the injected fluid being homogenous in composition (Fig. 3). In the case of Experiment A, clear stagnant zones develop at the lowest flow rates. However, both experiments clearly exhibit high-velocity zones along the edges of the slot. In the case of Experiment B, these features are present and stable at all injection rates. In this section, we investigate what mechanisms might explain the development and stability of such high-velocity channels with the slot. Using a CFD model, we attempted to match this behavior by introducing heterogeneity into the slot due to: (1) variations in aperture of the slot; (2) blockages in the manifold at the inlet and outlet; or (3) heterogeneity in the SVF field within the inlet manifold.

We use a Lagrangian particle-based approach for tracking the fluids and slurry within the fracture. Our model approximates a variable aperture fracture with a grid of square parallel plate cells. Within each cell, an approximation for fully-developed flow between the plates is used to establish relationships between the local pressure gradient and local slurry flux. The primary advantage of the fully-developed approximation is that we avoid the need to discretize through the thickness of the fracture and reduce the three-dimensional aperture space to a two-dimensional approximation which can be solved much more efficiently. More complete details of the numerical method may be found in Medina et al. [13].

Our measurements of aperture indicate that the variations in aperture within the slot are within several percent of the average at most and generally much less. Such small variations in aperture cannot explain doubling of the fluid velocity. Furthermore, the measured variations in aperture do not correlate with the high-velocity flow channels, thus ruling out the first hypothesis.

The effect of introducing blockages within the upstream and downstream manifolds through changes to the aperture field while assuming the slurry itself remains homogeneous were also investigated with our model. Using such a geometry, it is possible to capture details of the velocity field resembling the experiment near the inlet and the outlet. However, the dissipative nature of flow between two plates results in the flow becoming essentially uniform in the middle of the slot.

We finally consider the possibility that variations in upstream SVF can lead to stable heterogeneity in the flow field. This hypothesis assumes that changes induced either within the upstream tubing or within the upstream manifold induce systematic changes in the upstream SVF pumped into the slot. While the precise mechanism controlling this segregation has not been identified, we can investigate the implications for flow within the observed portion of the slot. For this hypothesis to be plausible, the induced changes should be relatively small. Furthermore, because the velocity distribution for Experiment B was independent of distance from the upstream inlet, the imposed changes in upstream SVF must propagate downstream through the slot without undergoing significant change.

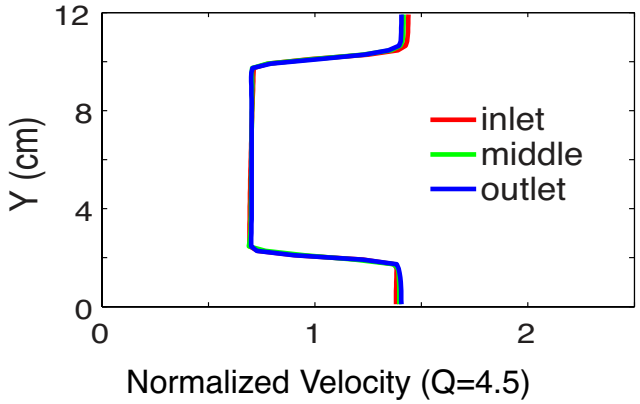


Fig. 7. Steady-state velocity profiles corresponding to a heterogeneous SVF model where it is assumed that there are variations in the upstream SVF. For low-SVF channels having an SVF of 0.47, the model predicts slurry velocities are approximately doubled in regions of approximately 2-cm width, in good agreement with experiment B (Fig. 4).

Our simulations assume a prescribed distribution of SVF at the upstream end of the slot corresponding to channels of approximately 2 cm width channels on either side. Our CFD models indicate that the imposed changes in the upstream SVF values are indeed preserved during flow, leading to sustained variations in the flow field downstream of the inlet manifold that persist all the way to the outlet manifold. In addition, our analysis indicates that a reduction of as little as 3% SVF can lead to an increase in velocity by a factor of two within the low-SVF channels over that in the higher-SVF central flow region (Fig. 7).

We conclude that only the third hypothesis is consistent with experimental observation. It appears likely that heterogeneity in the SVF field was induced within the upstream tubing and/or inlet manifold due to separation of the solids from the carrier fluid or sorting of the different-sized particles. Once such heterogeneity developed, our analysis indicates that such small changes in the SVF field are both stable and sufficient to induce large (factor of 2) variations in flow channels within the slot. Figure 8 explores the relationship between the velocity of the central region and the fast channels as we introduce progressively greater differences between the SVF of the two regions. For the same pressure drop across the slot we also calculated the corresponding total flux obtained for these heterogeneous scenarios compared with the total flux for a homogeneous slurry with SVF of 0.5 (red curve in Fig. 8). We see that even as the velocity ratio between the slow and fast channels approaches zero, the difference from the *total* flux predicted by the homogeneous theory is only tens of percent. These results suggest that bulk measurements, such as pressure drop and total flux through the slot, provide only weak constraint upon the nature of the flow within the slot. Specifically, very high velocity channels may develop within the slot while the total flux changes only slightly. However, other transport properties of the heterogeneous system, such as initial breakthrough of slurry and dispersion, will differ greatly from the homogeneous scenario.

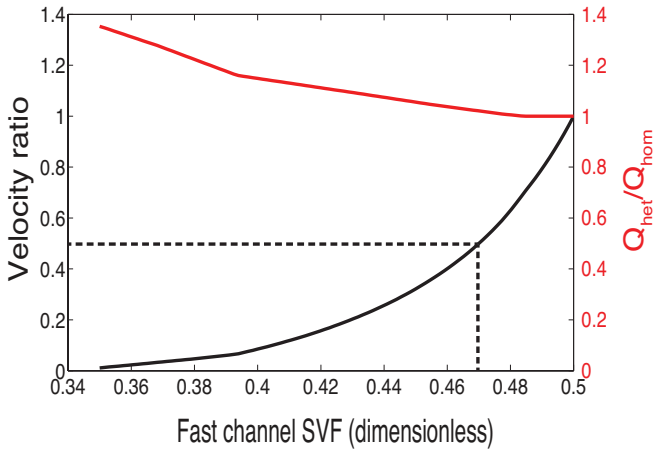


Fig. 8. We explore the influence of increasing SVF contrast in the slot upon the heterogeneity in the flow field. The black curve shows the predicted ratio of velocity in the central portion of the slot to two low-SVF channels of 2 cm width. We see that as the fast-channel SVF approaches 0.34, the flow in the central region stagnates. An SVF of 0.47 approximates the experimental observation of velocity doubling in the fast channel zones (a ratio of 0.5 on this plot). The red curve shows the ratio of total flux in the heterogeneous scenario compared with the flow of a homogeneous SVF of 0.5 for the same pressure drop across the slot. We see that even as the central region stagnates, the total flux differs from the homogeneous solution by only tens of percent.

## 6. CONCLUSION

We have demonstrated that the experimentally observed relationship between pressure drop and total flux is consistent with models of dense slurry flow within confined geometries. In addition, our analysis indicates that heterogeneity in the SVF field was most likely induced within the upstream tubing and/or inlet manifold due to separation of the solids from the carrier fluid or

sorting of the different-sized particles. Further analysis demonstrated that small changes (~3%) in the SVF field are both stable and sufficient to induce large (factor of 2) variations in flow channels within the slot. This result has implications for the transport of dense slurries within confined geometries, such as fractures and faults. Specifically, we have seen that any heterogeneity that develops within the density of the transported slurry will not necessarily be dissipated, but in fact may be propagated over long distances within the fracture/fault. Furthermore, as the slurry density approaches the critical limit, very small changes in SVF can result in large differences in the effective viscosity of the slurry and induce high-flux channels. Our experimental observations and modeling indicate that these channels may prove stable. Finally, while the actual flow within the fracture/fault may be highly heterogeneous, the average pressure drop and total flux through the system will remain close to that predicted for homogeneous flow. Consequently, while the assumption of uniform flow may match observations of pressure drop and total flux, it may greatly underestimate both the time of breakthrough and degree of dispersion of the slurry transported within the fracture.

## REFERENCES


1. Mader, H. M., E. W. Llewellin, and S. P. Mueller. 2013. The rheology of two-phase magmas: A review and analysis: Journal of Volcanology and Geothermal Research 257: 135–158.
2. Kern, L. R., T. K. Perkins, and R. E. Wyant. 1959. The Mechanics of Sand Movement in Fracturing: Transactions of the American Institute of Mining and Metallurgical Engineers 216: 403–405.
3. Montgomery, C. 2013. Fracturing Fluids, Effective and Sustainable Hydraulic Fracturing. Dr. Rob Jeffrey (Ed.), ISBN: 978-953-51-1137-5, InTech, DOI: 10.5772/56192. Available from: http://www.intechopen.com/books/effective-and-sustainable-hydraulic-fracturing/fracturing-fluids.
4. Murdoch, L. C., J. R. Richardson, Q. F. Tan, S. C. Malin and C. Fairbanks, C. 2006. Forms and sand transport in shallow hydraulic fractures in residual soil. *Canadian Geotechnical Journal* 43 (10): 1061–1073.
5. Lecampion, B., and D. Garagash. 2014. Confined flow of suspensions modeled by a frictional rheology: Journal of Fluid Mechanics. (submitted)
6. Cox, R. G., and S. G. Mason. 1971. Suspended Particles in Fluid Flow through Tubes. Annual Review of Fluid Mechanics 3: 291–316.
7. Lyon, M. K., and L. G. Leal. 1998. An experimental study of the motion of concentrated suspensions in two-dimensional channel flow. Part 1. Monodisperse systems: Journal of Fluid Mechanics 363: 25–56.
8. Deboeuf, A., G. Gauthier, J. Martin, Y. Yurkovetsky, and J. F. Morris. 2009. Particle Pressure in a Sheared Suspension: A Bridge from Osmosis to Granular Dilatancy. Physical Review Letters 102 (10): 108301-1–108301-4.
9. Boyer, F., E. Guazzelli, and O. Pouliquen. 2011. Unifying Suspension and Granular Rheology. *Physical Review Letters* 107 (18): 188301-1–188301-5.
10. Bittleston, S. H., J. Ferguson, and I. A. Frigaard. 2002. Mud removal and cement placement during primary cementing of an oil well - Laminar non-Newtonian displacements in an eccentric annular Hele-Shaw cell. *Journal of Engineering Mathematics* 43 (2–4): 229–253.
11. Detwiler, R. L., S. E. Pringle, and R. J. Glass, R. J. 1999. Measurement of fracture aperture fields using transmitted light: An evaluation of measurement errors and their influence on simulations of flow and transport through a single fracture: Water Resources Research 35 (9): 2605–2617.
12. Thielicke, W., and E. Stamuis. 2012. PIVLab—Time-resolved digital particle image velocimetry tool for MATLAB. Ver. 1.32. http://pivlab.blogspot.com/.
13. Medina, R., J. E. Elkhoury, J. P. Morris, R. Prioul, J. Desroches, and R. L. Detwiler, Flow of dense suspensions through fractures: Significant in-plane velocity variations caused by small variations in solid concentration, *Geofluids*. (in review)